

## Green's function molecular dynamics including viscoelasticity

van Dokkum, Jan; Nicola, Lucia

**DOI**

[10.1088/1361-651X/ab3031](https://doi.org/10.1088/1361-651X/ab3031)

**Publication date**

2019

**Document Version**

Final published version

**Published in**

Modelling and Simulation in Materials Science and Engineering

**Citation (APA)**

van Dokkum, J., & Nicola, L. (2019). Green's function molecular dynamics including viscoelasticity. *Modelling and Simulation in Materials Science and Engineering*, 27(7), Article 075006. <https://doi.org/10.1088/1361-651X/ab3031>

**Important note**

To cite this publication, please use the final published version (if applicable). Please check the document version above.

**Copyright**

Other than for strictly personal use, it is not permitted to download, forward or distribute the text or part of it, without the consent of the author(s) and/or copyright holder(s), unless the work is under an open content license such as Creative Commons.

**Takedown policy**

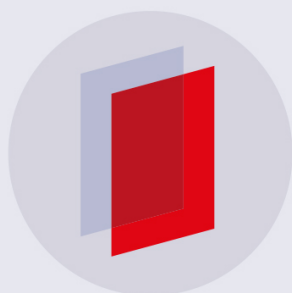
Please contact us and provide details if you believe this document breaches copyrights. We will remove access to the work immediately and investigate your claim.

PAPER • OPEN ACCESS

## Green's function molecular dynamics including viscoelasticity

To cite this article: Jan Steven van Dokkum and Lucia Nicola 2019 *Modelling Simul. Mater. Sci. Eng.* **27** 075006

View the [article online](#) for updates and enhancements.



**IOP | ebooks™**

Bringing you innovative digital publishing with leading voices to create your essential collection of books in STEM research.

Start exploring the collection - download the first chapter of every title for free.

# Green's function molecular dynamics including viscoelasticity

Jan Steven van Dokkum<sup>1</sup> and Lucia Nicola<sup>1,2</sup> 

<sup>1</sup> Department of Materials Science and Engineering, Delft University of Technology, 2628 CD Delft, The Netherlands

<sup>2</sup> Department of Industrial Engineering, University of Padova, 35131 Padua, Italy

E-mail: [l.nicola@tudelft.nl](mailto:l.nicola@tudelft.nl)

Received 4 March 2019, revised 1 July 2019

Accepted for publication 8 July 2019

Published 1 August 2019



CrossMark

## Abstract

The contact mechanical response of various polymers is controlled by the viscoelastic behavior of their bulk and the adhesive properties of their interface. Due to the interplay between viscoelasticity and adhesion it is difficult to predict the contact response, even more when surfaces are rough. Numerical modeling could be of assistance in this task, but has so far mostly dealt with either adhesion or viscoelasticity and focused on simple geometries. Ideally, one would need a model that can concurrently describe viscoelasticity, surface roughness, and interfacial interactions. The numerical technique named Green's function molecular dynamics (GFMD) has the potential to serve this purpose. To date, it has been used to model contact between adhesive elastic bodies with self-affine surfaces. Here, as a first step, we extend the GFMD technique to include the transient contact response of frictionless viscoelastic bodies. To this end, we derive the constitutive equation for a viscoelastic semi-infinite body in reciprocal space, then integrate it using the semi-analytical method, and find the quasi-static solution through damped dynamics of the individual modes. The new model is then applied to study indentation as well as rolling of a rigid cylinder on a frictionless isotropic half-plane that follows the Zener model when loaded in shear. Extension of the method to a generalized viscoelastic model is straightforward, but the computational effort increases with the number of time-scales required to describe the material. The steady-state response of the rolling cylinder was provided analytically by Hunter in the sixties. Here, we use his analytical solution to validate the steady-state response of our model and provide additionally the transient response for bodies with various shear moduli.



Original content from this work may be used under the terms of the [Creative Commons Attribution 3.0 licence](https://creativecommons.org/licenses/by/3.0/). Any further distribution of this work must maintain attribution to the author(s) and the title of the work, journal citation and DOI.

Keywords: viscoelasticity, Green's function, contact mechanics

(Some figures may appear in colour only in the online journal)

## 1. Introduction

The contact mechanics of viscoelastic materials is relevant, among other things, in the application of tires [1–3], pressure sensitive adhesives [4–6], conveyor belts [7, 8], and metrological devices [9–11]. In the presence of viscoelasticity the contact mechanical problem is significantly more complex compared to elasticity, since the material response is time-dependent [12]. The time dependence is responsible for phenomena that are not yet fully understood and controllable, such as adhesional hysteresis [13, 14], dissipative friction (e.g. viscoelastic dissipation) [2, 15] and the nonlinear leak rate of seals, o-rings and gaskets, near the contact percolation state [16]. The main challenge in tackling contact problems between viscoelastic bodies is that they involve a broad range of length- and time-scales that are difficult to deal with both experimentally and theoretically. The length-scales relate to the wavelengths required to describe the rough surfaces in contact, while the time-scales relate to the relaxation times of the viscoelastic materials, which span from milliseconds to hours.

Analytical solutions exist only for rather simple contact problems, e.g. frictionless indentation and rolling of Hertzian punches with smooth (no roughness) surfaces on viscoelastic bodies with mostly a single relaxation time [17–20]. To consider roughness and more sophisticated viscoelastic models, group renormalization theory [21, 22] and bearing-area models [15, 23] are used. The main drawback is that these approaches are only exact either at full or infinitesimal contact and that they do not account for adhesive interfaces. A feasible approach to describe accurately both the contact geometry, viscoelasticity at any relative contact area and interfacial interactions is to use numerical simulations.

Most numerical models involving viscoelasticity are restricted to studying the steady-state response under constant loading rate of frictional contacts [22, 24–30], while the most interesting phenomena are related to the transient response under reciprocating mixed-mode loading of adhesive contacts. While adhesive contact between elastic bodies is already extensively studied, e.g. [31–34], there is certainly a need for efficient computational techniques to model multi-length-scale roughness and viscoelasticity while accounting for interfacial interactions. To move a first step in this direction, we extend here the numerical technique known as Green's function molecular dynamics (GFMD) [35] to study the transient response of viscoelastic bodies. We choose the GFMD method because it gives a quick converging static solution for rough surfaces under contact loading [35, 36] and treats interfacial interactions simply through inter-atomic potentials [37]. This means that it forms an ideal platform to study adhesive viscoelastic contact problems under generic loading. An additional interesting feature of GFMD is that it can be used, similarly to the work by Pastewka and Robbins [38], to study contact problems where the surface is modeled through molecular statics and the rest of the body is modeled as a continuum. GFMD is used to simulate finite height slabs [39], compressible solids [40], contact between explicitly modeled deformable bodies and their interaction through a mixed-mode coupled cohesive zone model [41]. It is already extended to study the steady-state rolling of a viscoelastic half-space on a rigid rough surface [22]. However, the transient viscoelastic response is not yet incorporated.

Taking into account the transient response is computationally very demanding because it requires to keep track of all time-scales that describe the material. Additionally, the numerical time-step must be sufficiently small to capture the occurrence of sudden events, e.g. peeling

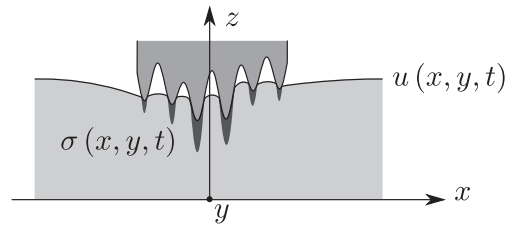


**Figure 1.** Schematic representation of a rigid punch indenting a viscoelastic half-space. Here,  $u(x, y, t)$  is the normal displacement of the rigid surface and  $\sigma(x, y, t)$  the normal contact stress at time  $t$ .

of small-scale asperities [14]. Koumi *et al* [42] studied the frictionless transient rolling contact of a rigid smooth Hertzian on a semi-infinite half-space with the boundary element method. More recently, Bugnicourt *et al* [43] were successful in modeling the transient response for the rolling of a viscoelastic material on a rough rigid surface using the fast Fourier transform boundary value method. They managed to predict the friction coefficient due to dissipative losses inside the viscoelastic bulk in tyre-road contact. Here, we focus on describing the trajectory of the surface grid points with higher accuracy than Bugnicourt *et al* [43] relying on the semi-analytical (SA) method [44] to integrate the equation of motion instead of the backwards Euler method [44]. This is achieved without a significant increase in computational cost.

In this work, the Green's function is obtained for an incompressible isothermal viscoelastic half-space loaded normally by a rigid cylinder. The constitutive equation is integrated through the SA method and the quasi-static solution is found through damped dynamics. As demonstrative case studies, we select the indentation and rolling of a rigid cylinder. This allows us to validate our model by comparison with the commercial finite-element software ABAQUS [45] and Hunter's analytical solution [18]. The finite element method is well suited for problems involving smooth contacts, while it becomes less appropriate than the model presented here for rough surfaces, as a large number of discretization points are needed. For the rolling cylinder the transient dissipative friction (caused by viscoelastic losses) and interfacial load are given for different rolling speeds and viscoelastic moduli.

## 2. Problem definition

A viscoelastic half-space is indented by a rigid punch, as schematically drawn in figure 1. The methodology presented in this section is valid for a punch with generic two-dimensional rough surface, although the examples solved subsequently in this work include only a cylindrical punch with smooth surface, treated in two-dimensions by means of a plane-strain analysis.

The contact mechanical problem, at time  $t$ , is governed by the following boundary conditions at the surface:

$$\begin{aligned} u(x, y, t) &= h(x, y) + u_z(t), \quad \text{for } (x, y) \in \Omega_c(t); \\ \sigma(x, y, t) &\neq 0, \quad \text{for } (x, y) \in \Omega_c(t); \\ \sigma(x, y, t) &= 0, \quad \text{for } (x, y) \notin \Omega_c(t), \end{aligned} \tag{1}$$

where  $u_z(t)$  is the indentation depth,  $h(x, y)$  the surface of the rigid punch and  $\Omega_c(t)$  the region in contact. Moreover, there is no externally applied shear traction so the only tangential traction is caused by the viscoelastic nature of the body.

The differential constitutive equation of a generic viscoelastic material at a given temperature reads

$$\sum_{i=0}^h p_i \frac{\partial^i \sigma(t)}{\partial t^i} = \sum_{j=0}^k q_j \frac{\partial^j \epsilon(t)}{\partial t^j}, \quad (2)$$

where  $\sigma(t)$  and  $\epsilon(t)$  are the stress and strain history tensor, and  $(p_i, q_j)$  are the material constants [46]. Decomposing the stress and strain history tensors in a hydrostatic ( $\sigma_0, \epsilon_0$ ) and deviatoric ( $s_{ij}, e_{ij}$ ) part one can write

$$\sum_{h=0}^l p_h^K \frac{\partial^h \sigma_0(t)}{\partial t^h} = \sum_{k=0}^r q_k^K \frac{\partial^k \epsilon_0(t)}{\partial t^k}, \quad \text{and} \quad \sum_{h=0}^m p_h^G \frac{\partial^h s_{ij}(t)}{\partial t^h} = \sum_{k=0}^n q_k^G \frac{\partial^k e_{ij}(t)}{\partial t^k}. \quad (3)$$

The four sums over the material constants are often expressed through symbolic operators  $P^K(t), Q^K(t), P^G(t), Q^G(t)$  of the type

$$P^K(t) = \sum_{h=0}^m p_h^K \frac{\partial^h}{\partial t^h}, \quad \text{and} \quad Q^K(t) = \sum_{k=0}^n q_k^K \frac{\partial^k}{\partial t^k}. \quad (4)$$

Here we assume that our viscoelastic material is elastic in dilatation and is described in shear by the Zener model [46]. The time-dependent shear modulus  $G(t)$  is defined by the Prony series expansion as

$$G(t) \equiv G_0 + \sum_{l=1}^{n'} G_l e^{-\frac{t}{T_l}}. \quad (5)$$

The instantaneous shear modulus  $G_{t \rightarrow 0}$ , the adiabatic shear modulus  $G_{t \rightarrow \infty}$ , the relaxation time  $T_l \equiv T_z$  and the retardation time  $\Theta_z$  are:

$$G_{t \rightarrow 0} = G_0 + G_1; \quad G_{t \rightarrow \infty} = G_0; \quad T_z = \frac{\eta}{G_1}; \quad \Theta_z = \left( \frac{1}{G_0} + \frac{1}{G_1} \right) \eta, \quad (6)$$

where  $G_0$  and  $G_1$  are the shear moduli and  $\eta$  the viscosity in the Zener model [46]. Combining equations (3)–(5), allows us to give the material constants as:

$$\begin{aligned} p_0^K &= 1; & q_0^K &= 3K; \\ p_0^G &= 1; & q_0^G &= 2G_0; \\ p_1^G &= \frac{\eta}{G_1}; & q_1^G &= 2 \frac{\eta(G_1 + G_0)}{G_1}, \end{aligned} \quad (7)$$

where  $K$  is the bulk modulus. Therefore, equation (3) takes the form:

$$\sigma_0 = 3K\epsilon_0, \quad \text{and} \quad s_{ij}(t) + \frac{\eta}{G_1} \dot{s}_{ij}(t) = 2G_0 e_{ij}(t) + 2 \frac{\eta(G_0 + G_1)}{G_1} \dot{e}_{ij}(t). \quad (8)$$

The rheological representation of the Zener model is given for reference in figure 2.

In Laplace space the equivalence between integral and differential expression of the constitutive relation allows one to relate the shear and bulk moduli to the symbolic operators as follows:

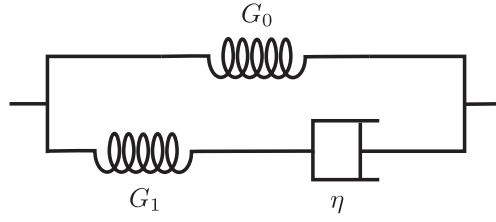


**Figure 2.** Rheological representation of the Zener model with shear moduli  $G_0$  and  $G_1$ , and viscosity  $\eta$ .

$$\bar{G}(s) = \frac{1}{2s} \frac{\bar{Q}^G(s)}{\bar{P}^G(s)}, \quad \text{and} \quad \bar{K}(s) = K, \quad (9)$$

where the Laplace transform  $\mathcal{L}\{\bullet(t)\} = \bar{\bullet}(s)$  of  $\bullet(t)$  is indicated by the over-bar, with  $s$  the complex frequency.  $\bar{P}^G(s)$  and  $\bar{Q}^G(s)$  have the same coefficients as the material constants in equation (3). For the Zener model  $\bar{G}(s)$  is:

$$\bar{G}(s) = \frac{1}{2s} \frac{q_0^G + q_1^G s}{p_0^G + p_1^G s}. \quad (10)$$

### 3. Solution through GFMD

In the GFMD technique, the surface of the deformable solid is discretized with  $n_x \times n_x$  equi-spaced grid points that interact with each other through an effective stiffness [35]. When the grid points are displaced by the indenter to a new configuration, the static elastic solution to the boundary value problem is obtained numerically in reciprocal space through damped dynamics [35, 36, 47]. The advantage of working in reciprocal space is that the stiffness matrix is symmetric and diagonal [41], so that each mode can be damped independently. For an *elastic* solid the areal elastic energy reads [47]:

$$v_{el}(t) = \frac{E^*}{4} \sum_{\mathbf{q}} |\mathbf{q}| |\tilde{u}(\mathbf{q}, t)|^2, \quad (11)$$

where  $\mathcal{F}\{\bullet(\mathbf{x})\} = \tilde{\bullet}(\mathbf{q})$  is the Fourier transform of  $\bullet(\mathbf{x})$ , with wave vector  $\mathbf{q}$ . As usual,  $E^* = E/(1 - \nu^2)$  is the effective modulus with  $E$  the elastic modulus and  $\nu$  the Poisson's ratio. The elastic normal stress corresponding to the wave vector  $\mathbf{q}$  at time  $t$  is

$$\tilde{\sigma}(\mathbf{q}, t) = -|\mathbf{q}| \frac{E^*}{2} \tilde{u}(\mathbf{q}, t). \quad (12)$$

Instead of an elastic material we here consider a solid elastic in dilatation and viscoelastic in shear. One can substitute  $E^*$  in equation (12) with the corresponding expression in terms of shear modulus  $G(t)$  and bulk modulus  $K$ ,

$$E(t) = \frac{9KG(t)}{3K + G(t)}, \quad \text{and} \quad \nu(t) = \frac{3K - 2G(t)}{6K + 2G(t)}. \quad (13)$$

We further assume that the solid is incompressible, so that  $K = E/(3 - 6\nu) \rightarrow \infty$ , and therefore:

$$\bar{\sigma}(\mathbf{q}, t) = -2|\mathbf{q}| G(t)\bar{u}(\mathbf{q}, t). \quad (14)$$

In virtue of the extended elastic–viscoelastic correspondence principle [48], we can find the solution to our viscoelastic boundary value problem relating the analytical Laplace transform of equation (14) and  $\bar{G}(s)$  in equation (10) as follows:

$$2(p_0^G + p_1^G s)\bar{\sigma}(\mathbf{q}, s) = -2|\mathbf{q}|(q_0^G + q_1^G s)\bar{u}(\mathbf{q}, s). \quad (15)$$

Substituting equation (7) of the Zener model in equation (15), taking the analytical inverse Laplace transform, and assuming that stress and displacement vanish for  $t \leq 0$ , we write the differential formulation for a given wave vector  $\mathbf{q}$  at time  $t$  as

$$\bar{\sigma}(\mathbf{q}, t) + \frac{\eta}{G_1}\dot{\bar{\sigma}}(\mathbf{q}, t) = -2|\mathbf{q}|\left(G_0\bar{u}(\mathbf{q}, t) + \frac{\eta(G_0 + G_1)}{G_1}\dot{\bar{u}}(\mathbf{q}, t)\right). \quad (16)$$

To use a more compact notation, we define  $C_{1,2,3,4}$  as the coefficient to the stress  $\bar{\sigma}(\mathbf{q}, t)$  and displacement  $\bar{u}(\mathbf{q}, t)$ , obtaining:

$$C_1\bar{\sigma}(\mathbf{q}, t) + C_2\dot{\bar{\sigma}}(\mathbf{q}, t) = -2|\mathbf{q}|\left(C_3\bar{u}(\mathbf{q}, t) + C_4\dot{\bar{u}}(\mathbf{q}, t)\right), \quad (17)$$

with  $C_1 = 1$  for the Zener model. The exact numerical integral solution of equation (17) requires the storage of the whole history of stresses and displacements and therefore becomes, with time, progressively more demanding in terms of memory and computational time. To reduce the computational effort, we opt for integrating the equation using the SA method. In the SA method, the simulation time is divided into  $n$  equal time periods of duration  $\Delta t$  over which equation (17) is integrated exactly, while the displacement rate is assumed to be constant [44, 49]. The stress in equation (17) can then be expressed as:

$$\bar{\sigma}(\mathbf{q}, t_n + \Delta t) = e^{-\frac{\Delta t}{C_2}}\bar{\sigma}(\mathbf{q}, t_n) - e^{-\frac{(t_n + \Delta t)}{C_2}} \int_{t_n}^{t_n + \Delta t} \frac{2|\mathbf{q}|e^{\frac{\tau}{C_2}}(C_3\bar{u}(\mathbf{q}, \tau) + C_4\dot{\bar{u}}(\mathbf{q}, \tau))}{C_2} d\tau, \quad (18)$$

where  $d\tau$  is the differential of time  $t$ ,

$$\dot{\bar{u}}(\mathbf{q}, t) = \frac{\bar{u}(\mathbf{q})_{t_n + \Delta t} - \bar{u}(\mathbf{q})_{t_n}}{\Delta t}, \quad \text{and} \quad \bar{u}(\mathbf{q}, t) = \bar{u}(\mathbf{q})_{t_n + \Delta t}. \quad (19)$$

The integration scheme for a given wave vector  $\mathbf{q}$  is

$$\bar{\sigma}(\mathbf{q})_{t_n + \Delta t} = e^{-\frac{\Delta t}{C_2}}\bar{\sigma}(\mathbf{q})_{t_n} - 2|\mathbf{q}|C_4\left(1 - e^{-\frac{\Delta t}{C_2}}\right)\left(\frac{\left(\frac{C_3\Delta t}{C_4} + 1\right)\bar{u}(\mathbf{q})_{t_n + \Delta t}}{\Delta t} - \frac{\bar{u}(\mathbf{q})_{t_n}}{\Delta t}\right). \quad (20)$$

When numerically evaluating the exponents on the right-hand side of equation (20), we use the Taylor-series expansion of the  $o$ th-order to prevent numerical rounding errors for small  $\Delta t/C_2$ .

The advantage of this method over exact numerical integration is that one only has to save the displacement  $\bar{u}(\mathbf{q})_{t_n}$  and stress  $\bar{\sigma}(\mathbf{q})_{t_n}$  across time-steps, contrary to saving the whole history of stresses and displacements. An alternative method to save computational resources is the backwards Euler process [44]. Our preference goes to the SA method because it has a second-order and up local error, where the backward Euler method has a zeroth-order and up error for the same  $\Delta t$ , as long as  $\Delta t \ll \Delta t_{\max} = \eta/(G_0 + G_1)$  [44]. The local error is defined

as the difference over a given time-step  $\Delta t$  between the Taylor-series expansions of the exact and integrated analytical solution. Note that the computational time required for the SA method is negligibly different from that required for the backward Euler method, since the only time difference is given by the one-time evaluation of the Taylor-series expansion.

The quasi-static solution at time  $t_n + \Delta t$  is obtained by solving the equation of motion for each mode with a unit mass in reciprocal space over a dimensionless time-step  $\Delta t^*$  via the position (Störmer-)Verlet (pSV) algorithm [50]. Note that the dimensionless time-step  $\Delta t^*$  is a numerical operator without any physical meaning while  $\Delta t$  has the dimension of time. The quasi-static solution is found quickest by critically damping each mode in reciprocal space. Hereby, we prevent overdamping the equation of motion through a non-monotonous adiabatic critical damping coefficient:

$$c_{\text{cr}} = 2\sqrt{2|q|G_0} - 2|q|G_0\Delta t^*. \quad (21)$$

In the limit  $\Delta t^* \rightarrow 0$ , the critical damping coefficient for the pSV is equivalent to that of an harmonic oscillator. When the *a priori* calculated dimensionless equilibrium time  $t_{\text{equil}}^*$  is reached, the stresses and displacements in reciprocal space are saved as input for the next dimensional time-step. A hard-wall boundary condition is applied in real space to prevent inter-penetration at the interface. The pseudo-code used to obtain the numerical results is presented in the [appendix](#).

#### 4. Numerical results: indentation by a rigid smooth cylinder

In this section, we aim at validating the newly developed viscoelastic GFMD method through comparison with results obtained using the commercial finite-element software ABAQUS [45]. Note that the finite element method is well suited to study the contact response of smooth bodies in contact, while for rough surfaces, where many discretization points are needed, the GFMD technique is computationally more efficient.

Simulations are performed in two-dimensions for a rigid smooth cylinder of radius  $R = \mathcal{L}/4$ , where  $\mathcal{L}$  is the periodic width of the simulation unit cell. The parabolic profile of the cylinder is

$$h(\rho) = \frac{R}{2} \left( \frac{\rho}{R} \right)^2, \quad (22)$$

where  $\rho$  is the distance from the vertical axis of symmetry.

The rigid indenter displaces as follows:

$$u_z(t) = \begin{cases} 0, & \text{for } t \leq 0; \\ -(h_0\mathcal{L}/T_z)t, & \text{for } 0 < t \leq T_z; \\ -h_0\mathcal{L}, & \text{for } t > T_z, \end{cases} \quad (23)$$

where the load  $h_0$  is defined as  $h_0 = -u_z(t \geq T_z)/\mathcal{L}$ . The maximum indentation depth is  $u_z^{\text{max}} = -0.05\mathcal{L}$ , in the small strain regime. In figure 3, we give the schematic representation of the case studied here.

The viscoelastic solid is taken to have height  $z_m$  large enough so that we can approximate its response as that of a semi-infinite solid. The average normal displacement of the surface  $u_m$  is

$$u_m = \frac{1 + \nu}{1 - \nu} \frac{1 - 2\nu}{E} \bar{p} z_m, \quad (24)$$

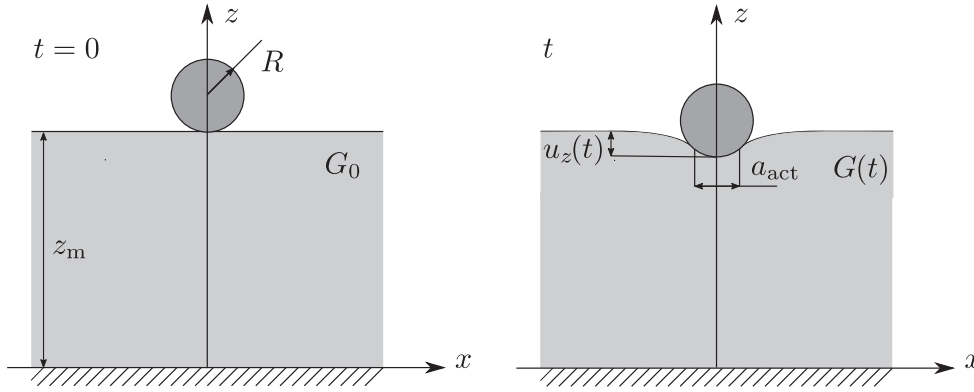


**Figure 3.** Schematic representation of the initial configuration and indentation by the rigid smooth cylinder to indentation depth  $u_z(t)$  and contact area  $a_{act}$ .

where  $\bar{p}$  is the mean contact pressure [51]. For the incompressible solids in this work the average displacement of the surface  $u_m$  is zero. Therefore, the GFMD simulations are performed assuming that the center-of-mass mode does not move. The surfaces in the GFMD simulations are discretized with  $n_x = 2^{14}$  equi-spaced grid points. The FEM simulations are performed, instead, for a finite sized unit cell of height  $z_m = \mathcal{L}$ , periodic in  $x$ -direction. The boundary of the square  $\mathcal{L} \times \mathcal{L}$  domain is discretized at the top with  $2^{13}$  equi-spaced nodes. The elements are irregular quadrilaterals and their shape and aspect ratio changes gradually depending on the region they discretize. In the region where the stress gradients are expected to be large the mesh is very fine and comprises elements with aspect ratio close to one. This zone has  $1.5a_{max}$  width at the top, where  $a_{max}$  is the contact area at maximum indentation depth, and has the same maximum depth, with a parabolic shape at its lower boundary. From there, the size of the elements increases gradually and reaches a larger aspect ratio at the bottom where the stress is homogeneous. The borders of the unit cell are discretized with  $2^9$  nodes, the bottom with  $2^7$  nodes.

The instantaneous shear modulus  $G_{t \rightarrow 0}$  is from now on indicated as  $G_\infty$  and the adiabatic shear modulus  $G_{t \rightarrow \infty}$  as  $G_0$  according to their respective frequency response. The ratio between instantaneous and long-time response to a step-load,  $G_\infty/G_0$  is taken to be 10, unless otherwise specified and the relaxation time  $T_z = 0.01$  s. Time in GFMD is discretized using  $(\Delta t_{max})/\Delta t = 50$ . This is sufficient to ensure convergence of the results. The isotropic rate-dependent material behavior in ABAQUS is described through the small-strain time domain viscoelastic material model (see [45]). The viscoelastic material is defined by a Prony series expansion of the dimensionless relaxation modulus, where the strain components are interpreted as state variables that control the stress relaxation. An *a priori* user-defined 0.001 strain error tolerance across dimensional time-steps is given [45, 46].

The change in relative contact area, defined as  $a_{rel} \equiv a_{act}/\mathcal{L}$ , and the reduced pressure  $p_r^* = \bar{p}/(4G_0\bar{g}_r)$ , where  $\bar{g}_r$  is the root mean square gradient over the contact area  $a_{act}$ , are reported in figures 4(a) and (b) as a function of time for the loads  $h_0 = 0.005, 0.01, 0.02$  and  $0.05$ . A good correspondence between the GFMD and FEM results is observed for loads up to  $h_0 = 0.02$ . For larger loads the discrepancy is given by the fact that the FEM unit cell has a large but finite height. When the cylinder is held constant for  $t \leq T_z$  the contact area becomes constant while the pressure decreases up to  $t/T_z \approx 6$ . At the hold the contact area

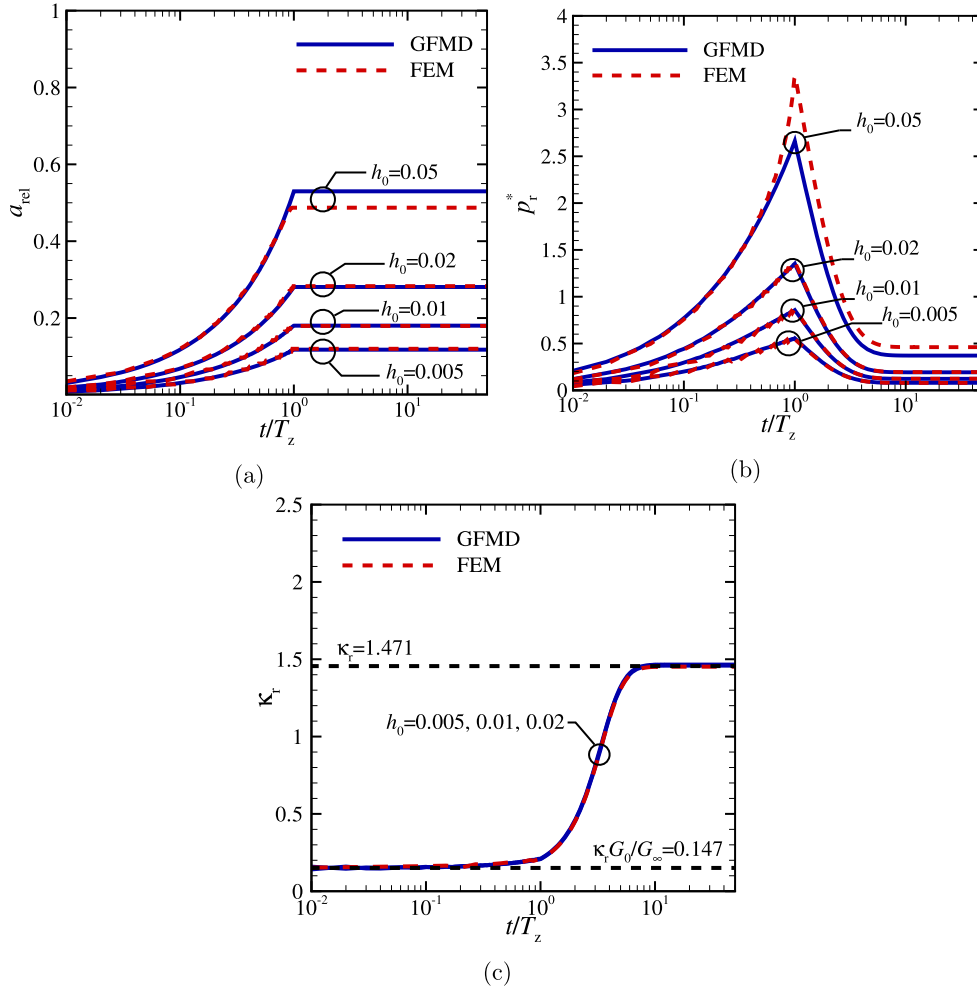


**Figure 4.** (a) The relative contact area  $a_{rel}$ , (b) the reduced pressure  $p_r^*$ , and (c) the proportionality coefficient  $\kappa_r$  as a function of the normalized time  $t/T_z$  for the loads  $h_0 = 0.005, 0.01, 0.02, 0.05$ .

does not change. This is in line with the analytical solution provided by Christensen [10] for the indentation by a rigid Hertzian.

Figure 4(c) shows the proportionality coefficient  $\kappa_r = a_{rel}/p_r^*$  as a function of the normalized time  $t/T_z$  for the three loads for which there is agreement between FEM and GFMD. The figure contains also the analytical values for the limiting cases of the instantaneous and steady-state proportionality coefficients,  $\kappa_r G_0/G_\infty = 0.147$  [52] and  $\kappa_r = 1.471$ , which show good correspondence with the numerical results. The method is thus validated for both its adiabatic and transient response.

#### 4.1. Numerical results: rolling of a rigid cylinder

The second problem we will consider is the frictionless rolling of a rigid cylinder on a semi-infinite incompressible viscoelastic solid, as depicted in figure 5. The steady-state

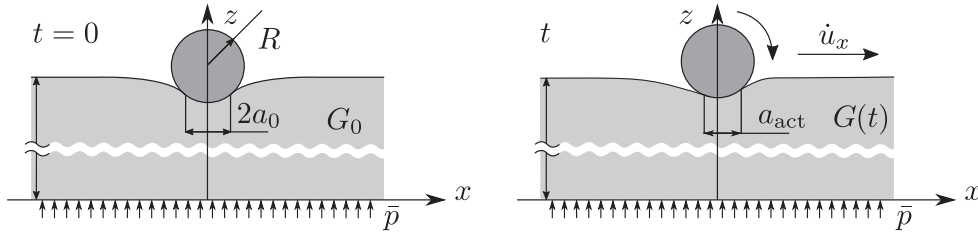


**Figure 5.** Schematic representation of the initial contact and subsequent rolling of the rigid smooth cylinder with tangential velocity  $\dot{u}_x$ .

analytical solution with which our results are compared was provided by Hunter [18]. The transient response is here given for the first time.

A far-field normal load,

$$L_n = \frac{\pi G_0 a_0^2}{R}, \quad (25)$$

is applied such as to ensure a relative adiabatic contact area  $a_{rel} = a_0/R = 1/4$ . The radius  $R = \mathcal{L}/10$  is selected to ensure no interaction between neighboring indenters. During rolling, the viscoelastic semi-infinite body experiences a displacing normal load but no tangential tractions, given that the interface is frictionless. However, due to the viscoelastic nature of the material, the displacements and the stress fields at any given moment depend on the tangential velocity  $\dot{u}_x$ . Therefore, a time-dependent tangential load  $L_t$  resists the frictionless sliding of the indenter. The tangential load is inferred from the local load balance as

$$L_t = \int_{a_{act}} \sigma(\rho) \frac{\partial h(\rho)}{\partial \rho} d\rho, \quad (26)$$

where  $a_{act}$  is the contact area. The dissipative friction coefficient  $\mu$  is defined as the ratio between the tangential and normal loads, i.e.  $\mu \equiv L_t/L_n$ . Note that here friction is only intended as the viscoelastic resistance of the bulk. Following Hunter [18], the normalized friction coefficient  $\mu R/a_0$  can be expressed as a function of the dimensionless velocity  $\dot{u}_x \Theta_z/a_0$ . Furthermore, we choose similarly to Hunter [18] the shear moduli  $G_\infty/G_0 = 2, 5, 10$  and prescribe the velocity  $\dot{U}_x(t) = H(t)(\dot{u}_x)$ , where  $H(t)$  is the Heaviside step-function.

In figure 6(a), the scaled steady-state normal load  $L/L_0$  is presented as a function of  $x/a_0$  for a cylinder moving with velocity  $\dot{u}_x \Theta_z/a_0 \approx 1$  on viscoelastic half-planes with constants  $G_\infty/G_0 = 1, 2, 5, 10$ . Here,  $L$  is the normal load on the surface at a given  $x$ -position and  $L_0$  is the adiabatic Hertzian normal load at  $x$ -position  $\rho = 0$ . The shear modulus ratio  $G_\infty/G_0 = 1$  corresponds to the adiabatic case, i.e. no viscous dissipation. The rolling direction is indicated by the black arrow pointing to the right.

The eccentricity of the load profile is found to increase with increasing  $G_\infty/G_0$ , so does the maximum value of the normal load. The results are in agreement with the analytical solution of Hunter 1961 [18], shown in figure 6(a) for  $G_\infty/G_0 = 2$ .

Notice that for the simulations just presented the contact area is not ever increasing with time, which is a necessary condition to invoke the elastic-viscoelastic correspondence principle that we used in section 3. The solution presented in section 3 can, however, also be obtained through the Boussinesq's equation in [43], which does not have the requirement of an ever increasing contact area, and can therefore be used also here.

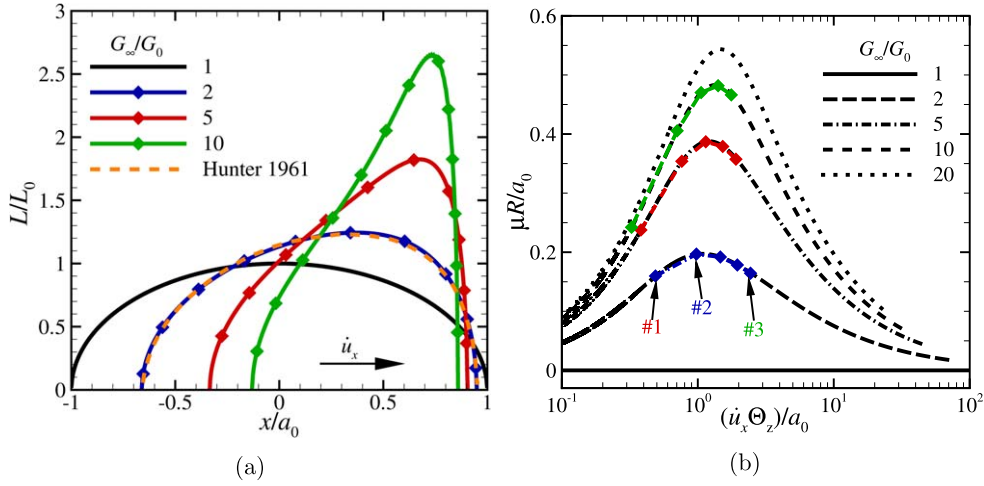


**Figure 6.** (a) The scaled steady-state normal load  $L/L_0$  as a function of the normalized  $x$ -position  $x/a_0$  with  $(\dot{u}_x \Theta_z)/a_0 \approx 1$  for  $G_\infty/G_0 = 1, 2, 5, 10$  and the analytical result by Hunter 1961 [18] for  $G_\infty/G_0 = 2$ . (b) Steady-state normalized friction coefficient  $\mu R/a_0$  as a function of the dimensionless velocity  $(\dot{u}_x \Theta_z)/a_0$  for various  $G_\infty/G_0 = 1, 2, 5, 10, 20$ . The black (dashed) lines are the analytical results by Hunter [18], the colored diamonds are numerical results and the colored dashed lines are guides to the eye.

In figure 6(b), the normalized friction coefficient  $\mu R/a_0$  is shown as a function of the dimensionless velocity  $\dot{u}_x \Theta_z/a_0$ . We observe good correspondence between all numerical results (colored diamonds) and the analytical result (black lines) by Hunter [18]. In line with the results in figure 6(a), the dissipative friction increases with increasing  $G_\infty/G_0$ . Furthermore, as expected [18, 24], the maximum dissipative friction is attained for  $\dot{u}_x \Theta_z/a_0 \approx 1$ , see for instance the point indicated with No. #2 for  $G_\infty/G_0 = 2$ . The other two points indicated on the same curve have the same friction coefficient at steady-state, but their transient dissipation is far from similar. This can be seen in figure 7(a), where  $\mu R/a_0$  is given as a function of  $t/\Theta_z$  for the rolling velocities  $\dot{u}_x \Theta_z/a_0$  corresponding to the points Nos. #1, #2 and #3 in figure 6(b). Constant dissipative friction coefficients are achieved after  $t/\Theta_z \approx 5$ . These are the steady-state values in figure 6(b). By increasing velocity  $\dot{u}_x$  from #1 to #3 the maximum transient dissipative friction  $\mu_{\max}$  increases and the time  $t/\Theta_z$  at which the maximum is observed, decreases.

In figure 7(b) the loads  $L/L_0$  corresponding to the maximum transient dissipative friction  $\mu_{\max}$ , indicated in figure 7(a) by colored circles, are presented as a function of  $x/a_0$ . The maximum normal load on the surface as well as the eccentricity of the load profile  $L(x/a_0)$  increase with increasing velocity  $\dot{u}_x$  (from A to C). This agrees once more with the increase in the maximum transient dissipative friction  $\mu_{\max}$  from the normalized time C to B and down to normalized time A in figure 7(a).

For all rolling velocities and shear moduli studied here it is found that: (1) The maximum transient dissipative friction coefficient  $\mu_{\max}$  increases with velocity  $\dot{u}_x \Theta_z/a_0$  for all shear moduli  $G_\infty/G_0 \neq 1$ ; (2) The maximum transient dissipative friction coefficient  $\mu_{\max}$  is larger than the steady-state friction coefficient for all velocities  $\dot{u}_x \Theta_z/a_0$  studied. The maximum observed in the transient friction coefficient  $\mu_{\max}$  corresponds to the stiction spike observed in the analytical work presented by Persson and Volokitin [21] and in the simulations of

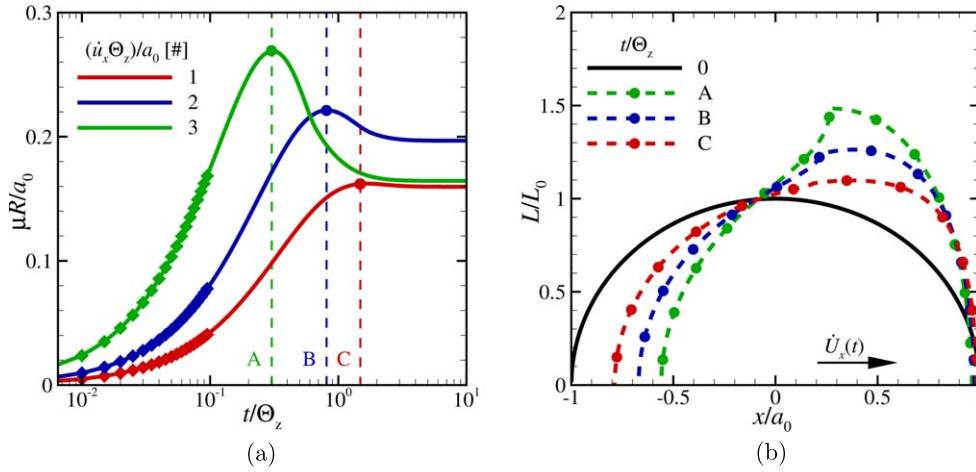


**Figure 7.** (a) Normalized friction coefficient  $\mu R/a_0$  as a function of  $t/\Theta_z$  with  $G_\infty/G_0 = 2$  and  $(\dot{u}_x \Theta_z)/a_0$  indicated in figure 6(b) by Nos. #1, #2 and #3. The data points are shown with colored diamonds only up to  $t/\Theta_z = 0.1$  for clarity. (b) The scaled normal load  $L/L_0$  as a function of  $x/a_0$  for  $t/\Theta_z$  indicated in (a) by A, B and C.

Bugnicourt *et al* [43]. The maximum is caused by the sudden increase in rolling velocity at time  $t = 0$ , and is largest for the largest initial velocity step. A similar increase in the static friction coefficient, although in the presence of adhesion at the surface, was measured in the experiments of Roberts and Thomas [53]. In their work, soft polymers show a large increase in friction coefficient compared to hard polymers. The authors observed a strong contribution of viscoelasticity to the overall frictional response for soft polymers. In our work, since the interface is frictionless, the only contribution to friction is provided by the viscoelastic response of the half-plane.

## 5. Concluding remarks

There is the need for efficient computational techniques to model multi-length-scale roughness and viscoelasticity while accounting for interfacial interactions. As a first step in this direction, we derive the Green's function for a quasi-static incompressible isothermal viscoelastic half-space. We implement the SA method as time-integration scheme [44] to obtain a fast and accurate solution of the equations of motion. The extension to the GFMD method provided in this work allows one to predict the transient and steady-state response of frictionless contacts.

The model is here applied to study the frictionless indentation and rolling of a smooth infinitely long rigid cylinder on a viscoelastic half-plane. These simple problems provide the means of validating the new method through comparison with results obtained by the finite element method and Hunter's analytical work. Additionally, the transient response upon rolling of the cylinder is here given for the first time.

The GFMD method presented and validated in this work provides a platform to model adhesion contacts in future work. This is needed as most interesting phenomena are related to the transient response under reciprocating mixed-mode loading of adhesive contacts, e.g. peeling of pressure sensitive adhesives.

## Acknowledgments

LN acknowledges funding from the European Research Council (ERC) under the European Union's Horizon 2020 research and innovation programme (Grant Agreement No. 681813).

## Appendix. Viscoelastic GFMD pseudo-code

- (i) Setup rigid indenter with initial surface topography  $h(x)_{t_n=0}$ ;
- (ii) Determine damping coefficient  $c_{cr}(q)$  such that all modes are critically damped and calculate the dimensionless equilibrium time  $t_{equil}^*$  for a given dimensionless time-step  $\Delta t^*$ ;
- (iii) Loop over  $n$  iterations with time-step  $\Delta t$  until  $t_{final}$  is reached. Give the location of the rigid indenter as  $h(x)_{t_n+\Delta t}^{punch} = h(x - u_{t_n+\Delta t}^x)_{t_n=0} + u_{t_n+\Delta t}^z$ , where  $u_{t_n+\Delta t}^z$  and  $u_{t_n+\Delta t}^x$  are the normal and tangential displacement of the indenter at time  $t_n + \Delta t$ .
  - (a) Loop over  $\Delta t^*$  until the dimensionless equilibrium time  $t_{equil}^*$  is reached;
    1. Discrete fast Fourier transform (DFFT) surface displacement  $u(x)_{t_n+\Delta t}^{now}$  using the FFTW3 library [54];
    2. Calculate viscoelastic restoring force:  
 $\tilde{F}(q)_{t_n+\Delta t}^{viscoelastic} \leftarrow \text{Function}\{\tilde{u}(q)_{t_n+\Delta t}^{now}, \tilde{u}(q)_{t_n}, \tilde{F}(q)_{t_n}, \Delta t\}$ ;
    3. Add external force and interfacial force,  
 $\tilde{F}(q)_{t_n+\Delta t}^{total} = \tilde{F}(q)_{t_n+\Delta t}^{viscoelastic} + \tilde{F}(q)_{t_n+\Delta t}^{ext} + \tilde{F}(q)_{t_n+\Delta t}^{if}$  ;
    4. Add damping forces,  $\tilde{F}(q)_{t_n+\Delta t}^d = \tilde{F}(q)_{t_n+\Delta t}^{total} - c_{cr}(q) \frac{\tilde{u}(q)_{t_n+\Delta t}^{now} - \tilde{u}^{old}(q)_{t_n+\Delta t}}{\Delta t^*}$ ;
    5. Use pSV to solve equation of motion,  
 $\tilde{u}(q)_{t_n+\Delta t}^{new} = 2\tilde{u}(q)_{t_n+\Delta t}^{now} - \tilde{u}(q)_{t_n+\Delta t}^{old} + \tilde{F}(q)_{t_n+\Delta t}^d (\Delta t^*)^2$ ;
    6. Assign  $\tilde{u}(q)_{t_n+\Delta t}^{old} \leftarrow \tilde{u}(q)_{t_n+\Delta t}^{now}$  and  $\tilde{u}(q)_{t_n+\Delta t}^{now} \leftarrow \tilde{u}(q)_{t_n+\Delta t}^{new}$ ;
    7. Reverse DFFT displacement  $u(q)_{t_n+\Delta t}^{now}$  into real space, and scale displacement  $u(x)_{t_n+\Delta t}^{now}$  with  $1/\mathcal{L}$ ;
    8. Implement the hard-wall  $u(x)_{t_n+\Delta t}^{now} \leftarrow \min\{u(x)_{t_n+\Delta t}^{now}, h(x)_{t_n+\Delta t}^{punch}\}$ ;
    9. Calculate interfacial force  $F(x)_{t_n+\Delta t}^{if} \leftarrow \text{Function}\{u(x)_{t_n+\Delta t}^{now}, h(x)_{t_n+\Delta t}^{punch}\}$  and DFFT to  $\tilde{F}(q)_{t_n+\Delta t}^{if}$ .
  - (b) DFFT displacement  $u(x)_{t_n+\Delta t}^{now}$ ;
  - (c) Save  $\tilde{u}(q)_{t_n} \leftarrow \tilde{u}(q)_{t_n+\Delta t}^{now}$  and  $\tilde{F}(q)_{t_n} \leftarrow \tilde{F}(q)_{t_n+\Delta t}^{total}$ .

## ORCID iDs

Lucia Nicola  <https://orcid.org/0000-0003-0873-4562>

## References

- [1] Le Gal A and Klüppel M 2007 Investigation and modelling of rubber stationary friction on rough surfaces *J. Phys.: Condens. Matter* **20** 015007
- [2] Tiwari A, Miyashita N, Espallargas N and Persson B N 2018 Rubber friction: the contribution from the area of real contact *J. Chem. Phys.* **148** 224701
- [3] Lang A and Klüppel M 2017 Influences of temperature and load on the dry friction behaviour of tire tread compounds in contact with rough granite *Wear* **380** 15–25

- [4] Krick B A, Vail J R, Persson B N and Sawyer W G 2012 Optical *in situ* micro tribometer for analysis of real contact area for contact mechanics, adhesion, and sliding experiments *Tribol. Lett.* **45** 185–94
- [5] Villey R, Ciccotti M, Creton C, Cortet P-P and Yarusso D J 2015 Influence of large strain rheology on the peeling performances of pressure sensitive adhesives *APS March Meeting Abstracts*
- [6] Chopin J, Villey R, Yarusso D, Barthel E, Creton C and Ciccotti M 2018 Nonlinear viscoelastic modeling of adhesive failure for polyacrylate pressure-sensitive adhesives *Macromolecules* **51** 8605–10
- [7] Wheeler C 2006 Indentation rolling resistance of belt conveyors-a finite element solution *Bulk Solids Handling* **26** 40–3
- [8] Robinson P and Wheeler C 2016 The indentation rolling resistance of spherically profiled idler rolls *Int. J. Mech. Sci.* **106** 363–71
- [9] Baek D, Saito S and Takahashi K 2018 Estimating work of adhesion using spherical contact between a glass lens and a PDMS block *J. Adhes. Sci. Technol.* **32** 158–72
- [10] Liu Z, Lu H, Zheng Y, Tao D, Meng Y and Tian Y 2018 Transient adhesion in a non-fully detached contact *Sci. Rep.* **8** 6147
- [11] Koumoulos E, Tofail S A, Silién C, De Felicis D, Moscatelli R, Dragatogiannis D, Bemporad E, Sebastiani M and Charitidis C 2018 Metrology and nano-mechanical tests for nano-manufacturing and nano-bio interface: challenges and future perspectives *Mater. Des.* **137** 446–62
- [12] Christensen R M 1982 *Theory of Viscoelasticity* (New York: Dover Publications)
- [13] Tiwari A, Dorogin L, Bennett A, Schulze K, Sawyer W, Tahir M, Heinrich G and Persson B 2017 The effect of surface roughness and viscoelasticity on rubber adhesion *Soft Matter* **13** 3602–21
- [14] Dorogin L and Persson B N 2018 Contact mechanics for polydimethylsiloxane: from liquid to solid *Soft Matter* **14** 1142–8
- [15] Popov V L, Voll L, Kusche S, Li Q and Rozhkova S V 2018 Generalized master curve procedure for elastomer friction taking into account dependencies on velocity, temperature and normal force *Tribol. Int.* **120** 376–80
- [16] Tiwari A, Dorogin L, Tahir M, Stöckelhuber K W, Heinrich G, Espallargas N and Persson B N 2017 Rubber contact mechanics: adhesion, friction and leakage of seals *Soft Matter* **13** 9103–21
- [17] Hunter S 1960 Hertz problem for a rigid spherical indenter and a viscoelastic half-space *J. Mech. Phys. Solids* **8** 219–34
- [18] Hunter S 1961 The rolling contact of a rigid cylinder with a viscoelastic half space *J. Appl. Mech.* **28** 611–7
- [19] Ting T 1966 The contact stresses between a rigid indenter and a viscoelastic half-space *J. Appl. Mech.* **33** 845–54
- [20] Ting T 1968 Contact problems in the linear theory of viscoelasticity *J. Appl. Mech.* **35** 248–54
- [21] Persson B N and Volokitin A 2002 Theory of rubber friction: nonstationary sliding *Phys. Rev. B* **65** 134106
- [22] Scaraggi M and Persson B 2015 Friction and universal contact area law for randomly rough viscoelastic contacts *J. Phys.: Condens. Matter* **27** 105102
- [23] Popov V L and Heß M 2015 *Method of Dimensionality Reduction in Contact Mechanics and Friction* (Berlin: Springer)
- [24] Persson B 2010 Rolling friction for hard cylinder and sphere on viscoelastic solid *Eur. Phys. J. E* **33** 327–33
- [25] Carbone G and Putignano C 2013 A novel methodology to predict sliding and rolling friction of viscoelastic materials: theory and experiments *J. Mech. Phys. Solids* **61** 1822–34
- [26] Scaraggi M and Persson B N 2014 Rolling friction: comparison of analytical theory with exact numerical results *Tribol. Lett.* **55** 15–21
- [27] Menga N, Putignano C, Carbone G and Demelio G 2014 The sliding contact of a rigid wavy surface with a viscoelastic half-space *Proc. R. Soc. A* **470** 20140392
- [28] Carbone G and Putignano C 2014 Rough viscoelastic sliding contact: theory and experiments *Phys. Rev. E* **89** 032408
- [29] Putignano C, Carbone G and Dini D 2015 Mechanics of rough contacts in elastic and viscoelastic thin layers *Int. J. Solids Struct.* **69** 507–17
- [30] Menga N, Afferrante L, Demelio G and Carbone G 2018 Rough contact of sliding viscoelastic layers: numerical calculations and theoretical predictions *Tribol. Int.* **122** 67–75

- [31] Pohrt R and Popov V L 2015 Adhesive contact simulation of elastic solids using local mesh-dependent detachment criterion in boundary elements method *Facta Univ., Ser.: Mech. Eng.* **13** 3–10
- [32] Popov V L, Pohrt R and Li Q 2017 Strength of adhesive contacts: influence of contact geometry and material gradients *Friction* **5** 308–25
- [33] Rey V, Anciaux G and Molinari J-F 2017 Normal adhesive contact on rough surfaces: efficient algorithm for FFT-based BEM resolution *Comput. Mech.* **60** 69–81
- [34] Bugnicourt R, Sainsot P, Dureisseix D, Gauthier C and Lubrecht A 2018 FFT-based methods for solving a rough adhesive contact: description and convergence study *Tribol. Lett.* **66** 29
- [35] Campañá C and Müser M H 2006 Practical Green's function approach to the simulation of elastic semi-infinite solids *Phys. Rev. B* **74** 075420
- [36] Campañá C and Müser M H 2007 Contact mechanics of real versus randomly rough surfaces: a Green's function molecular dynamics study *Europhys. Lett.* **77** 38005
- [37] Müser M H 2014 Single-asperity contact mechanics with positive and negative work of adhesion: influence of finite-range interactions and a continuum description for the squeeze-out of wetting fluids *Beilstein J. Nanotechnol.* **5** 419
- [38] Pastewka L, Sharp T A and Robbins M O 2012 Seamless elastic boundaries for atomistic calculations *Phys. Rev. B* **86** 075459
- [39] Carbone G and Mangialardi L 2008 Analysis of the adhesive contact of confined layers by using a Green's function approach *J. Mech. Phys. Solids* **56** 684–706
- [40] Venugopalan S P, Nicola L and Müser M H 2017 Green's function molecular dynamics: including finite heights, shear, and body fields *Modell. Simul. Mater. Sci. Eng.* **25** 034001
- [41] Salehani M K, Irani N, Müser M and Nicola L 2018 Modelling coupled normal and tangential tractions in adhesive contacts *Tribol. Int.* **124** 93–101
- [42] Koumi K E, Chaise T and Nelias D 2015 Rolling contact of a rigid sphere/sliding of a spherical indenter upon a viscoelastic half-space containing an ellipsoidal inhomogeneity *J. Mech. Phys. Solids* **80** 1–25
- [43] Bugnicourt R, Sainsot P, Lesaffre N and Lubrecht A 2017 Transient frictionless contact of a rough rigid surface on a viscoelastic half-space *Tribol. Int.* **113** 279–85
- [44] Sorvari J and Hämäläinen J 2010 Time integration in linear viscoelasticity a comparative study *Mech. Time-Dep. Mater.* **14** 307–28
- [45] Hibbitt H D, Karlsson B I and Sorensen E P 2001 *ABAQUS User's Manual* vol 1
- [46] Marques S P and Creus G J 2012 *Computational Viscoelasticity* (New York: Springer)
- [47] Prodanov N, Dapp W B and Müser M H 2014 On the contact area and mean gap of rough, elastic contacts: dimensional analysis, numerical corrections, and reference data *Tribol. Lett.* **53** 433–48
- [48] Graham G 1968 The correspondence principle of linear viscoelasticity theory for mixed boundary value problems involving time-dependent boundary regions *Q. Appl. Math.* **26** 167–74
- [49] Taylor R L, Pister K S and Goudreau G L 1970 Thermomechanical analysis of viscoelastic solids *Int. J. Numer. Methods Eng.* **2** 45–59
- [50] Störmer C 1912 Sur les trajectoires des corpuscules électrisés dans l'espace sous l'action du magnétisme terrestre, avec application aux aurores boréales *Le Radium* **9** 395–9
- [51] Menga N, Afferrante L and Carbone G 2016 Effect of thickness and boundary conditions on the behavior of viscoelastic layers in sliding contact with wavy profiles *J. Mech. Phys. Solids* **95** 517–29
- [52] van Dokkum J, Salehani M K, Irani N and Nicola L 2018 On the proportionality between area and load in line contacts *Tribol. Lett.* **66** 115
- [53] Roberts A and Thomas A 1977 Static friction of smooth clean vulcanized rubber *Rubber Chem. Technol.* **50** 266–71
- [54] Frigo M and Johnson S G 2005 The design and implementation of FFTW3 *Proc. IEEE* **93** 216–31